Thermodynamic guiding principles of high-capacity phase transformation materials for splitting H_2O and CO_2 by thermochemical looping

Thermodynamic guiding principles of high-capacity phase transformation materials for splitting H_2O and CO_2 by thermochemical looping

Shang Zhai[1,*], Joonhyun Nam[2], Gopalakrishnan Sai Gautam[3,†], Kipil Lim[4,5], Jimmy Rojas[1], Michael F. Toney[6], Emily A. Carter[3,7], In-Ho Jung[2], William C. Chueh[4,8,9], Arun Majumdar[1,8]

[1] Department of Mechanical Engineering, Stanford University, Stanford, CA 94305, USA.

[2] Department of Materials Science and Engineering, Seoul National University, Seoul, 08826, South Korea.

[3] Department of Mechanical and Aerospace Engineering, Princeton University, Princeton, NJ 08544, USA.

[4] Department of Materials Science and Engineering, Stanford University, Stanford, CA 94305, USA.

[5] Stanford Synchrotron Radiation Lightsource, SLAC National Accelerator Laboratory, Menlo Park, CA 94025, USA.

[6] Department of Chemical and Biological Engineering, University of Colorado Boulder, Boulder, CO 80309, USA.

[7] Office of the Chancellor and Department of Chemical and Biomolecular Engineering, University of California, Los Angeles, CA 90095, USA.

[8] Precourt Institute for Energy, Stanford University, Stanford, CA 94305, USA.

[9] Applied Energy Division, SLAC National Accelerator Laboratory, Menlo Park, CA 94025, USA.

[*] Corresponding author: shangz@stanford.edu

[†] Present address: Department of Materials Engineering, Indian Institute of Science, Malleshwaram, Bengaluru, Karnataka 560012, India.

Abstract

Thermochemical looping splitting of water and carbon dioxide (CO_2) with greenhouse-gas-free (GHG-free) energy has the potential to help address the Gt-scale GHG emissions challenge. Reaction thermodynamics largely contributes to the main bottlenecks of cost reduction for thermochemical looping water/CO_2 splitting cycle. Here, we analyze thermodynamic driving forces in such cycles with two-phase ternary ferrites as model systems. We find that cation configurational entropy chiefly determines the change of partial molar entropy with oxygen stoichiometry. In addition, our phase diagram analysis accurately predicts the optimal Fe ratio for maximal water/CO_2 splitting capacity in thermal reduction and in chemical reduction based cycles, underlining the significance of phase boundary positions. With chemical reduction, >10% CO_2 conversion and high oxygen exchange capacity can both be achieved. Furthermore, our reduced Gibbs free energy model illustrates critical thermodynamic factors that influence the water/CO_2 splitting capacity. Our research reveals the thermodynamic driving forces underlying the unconventional high-capacity Fe-poor ferrites, further explained via phase diagrams of Fe-Co-O, Fe-Ni-O and Fe-Mg-O. Future materials improvements can be guided by our reduced Gibbs free energy model.
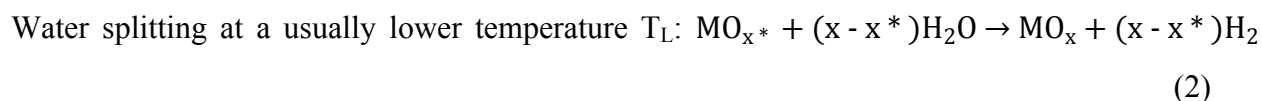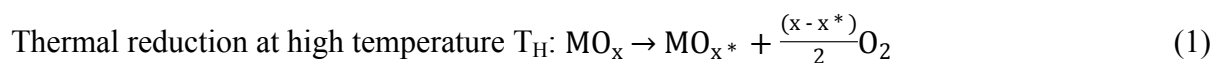
Introduction

Greenhouse gases (GHGs) are now being emitted globally at a rate of ~50 Gt-CO_2-equivalent per year from transportation, electricity/heat production, industry, agriculture and land use [1]. As a result, atmospheric carbon dioxide (CO_2) concentration recently has gone beyond 400 ppm, while it never exceeded 300 ppm before the industrial revolution [2]. To hold "the increase in global average temperature to well below 2°C above pre-industrial levels" [3-8], the net emission of GHGs from human activities needs to reduce to negligible or negative levels in the upcoming decades [9,10].

A promising way to lower GHG emissions is to produce GHG-free hydrogen (H_2) at around \$1/kg cost, which would be competitive with its production via steam reforming of fossil fuels [11]. Low-cost, Gt-scale and GHG-free H_2 can help decarbonize industrial heat and feedstocks (e.g., heat needed to make steel, cement, ammonia, and hydrogen feedstock for ammonia, petrochemical, and biofuel industries) and potentially transportation (biofuel vehicles and heavy-duty hydrogen vehicles), and it can also act as an energy storage medium for intermittent renewables [12]. Using GHG-free energy, water splitting can produce GHG-free H_2 through electrolysis [13-15], photo(electro)chemistry [16] and artificial photosynthesis [17]. While these routes have advantages such as flexibility, mild conditions, and reasonably high efficiency, it is noteworthy that the chemical infrastructure today at the Gt-scale relies almost exclusively on thermochemical processes. Hence, such dominance of thermochemistry warrants research in creating options for thermochemical looping water splitting to leverage existing industrial expertise.

Another approach to help achieve the GHG emission reduction goal is synthetic transformation of CO_2 into chemicals and fuels, which can offer the potential for emission reductions and even negative emissions [18-25]. Splitting CO_2, a relatively stable molecule, into oxygen (O_2) and carbon monoxide (CO), a more energy-rich molecule that can form the basis for organic compounds including hydrocarbon fuels [20], is a critical first step to transforming CO_2. Similar to the discussion above on water splitting routes, thermochemical looping CO_2 splitting has the promise of leveraging the Gt-scale chemical infrastructure today.

Chemical looping breaks down a target reaction into several reactions and it is a versatile platform technology to produce heat and chemicals [26–29]. Such cyclic processes often involve a solid material going through thermochemical reactions. Hydrogen production research and development include several examples of chemical looping with a metal oxide as an oxygen carrier.

When the metal oxide is reduced by increasing temperature, the chemical looping water splitting usually refers to two-step thermochemical water splitting [30–35]. Here a metal oxide (MO_x, where M can be a combination of multiple metal cations) goes through two oxygen exchange reactions:

Thermal reduction at high temperature T_H: $MO_x \rightarrow MO_{x*} + \frac{(x-x^*)}{2}O_2$ (1)

Water splitting at a usually lower temperature T_L: $MO_{x*} + (x-x^*)H_2O \rightarrow MO_x + (x-x^*)H_2$ (2)

And the net reaction is $\left[H_2O \rightarrow \frac{1}{2}O_2 + H_2 \right](x - x^*)$

Instead of the thermal reduction in (1), the metal oxide also can be reduced chemically at a temperature usually lower than T_H. Commonly investigated reducing agents include coal and natural gas[28,36–41]. CO_2 emission from the reduction reaction needs to be avoided by measures like CO_2 capture and sequestration to achieve GHG-free splitting of water/CO_2. Taking CH_4 as an example:

Chemical reduction at temperature $T_{Looping}$:

$MO_x + \frac{(x-x^*)}{4}CH_4 \rightarrow MO_{x*} + \frac{(x-x^*)}{2}H_2O + \frac{(x-x^*)}{4}CO_2$ (3)
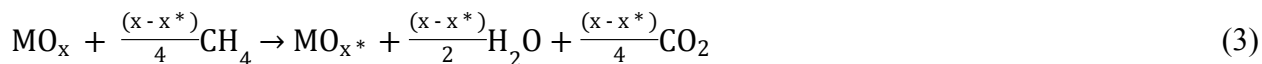
Additionally, instead of the water splitting in (2), MO_{x*} alternatively can split CO_2 into CO [42]:

CO_2 splitting at T_L: $MO_{x*} + (x-x^*)CO_2 \rightarrow MO_x + (x-x^*)CO$ (4)

In chemical reduction based thermochemical looping cycles, T_L is usually the same as $T_{Looping}$.

The CO_2 splitting thermochemical looping cycles (with either thermal reduction or chemical reduction) are used for analyses in this paper unless otherwise noted. Since the reaction thermodynamics is very similar between water and CO_2 splitting [43,44], the analysis and conclusions are applicable to both situations.

The main technological requirements for lowering the product cost in the thermochemical looping cycle include: 1) large thermodynamic equilibrium CO_2/water splitting capacity ([45]; defined in **Subsection 1 of Results and discussion**) at feasible conditions, usually described as a large oxygen release from the oxide at a practical temperature and oxygen partial pressure (p_{O_2}) [46], and a high CO_2/water conversion; 2) fast reaction kinetics that enables a short cycle time [47–49]; and 3) long-term cyclability of both the reactor and the redox material.

Reaction thermodynamics affects many of the bottlenecks above. For reactions (1) - (4) to proceed (i.e., have a negative Gibbs free energy change), we derived constraints with respect to the partial molar enthalpy (h_O) and entropy (s_O) of oxygen for MO_x (**Subsection 1 of Results and discussion**). Common metal oxides for two-step thermochemical CO_2/water splitting have h_O spanning a large range but s_O is usually lower than needed [43,44]. Therefore, analyzing the source and change of s_O is critical for directing materials design. For example, a strategy of simultaneous cation redox in a perovskite was reported to increase absolute s_O [50].

Recently, iron(Fe)-poor ferrite ($Fe_yM_{1-y}O_x$ where y < 2/3) was found to have a counterintuitively high capacity of CO_2 splitting compared to the traditional Fe-rich ferrites (y ≥ 2/3) in the two-step thermochemical cycle (with thermal reduction) [51]. Even more recently, in the case of thermochemical looping hydrogen production with chemical reduction, various Fe-poor ferrites were shown to have much higher capacity and water-to-H_2 conversion compared to the benchmark material, Fe_3O_4-FeO-Fe [52]. Technoeconomic analysis suggests that such Fe-poor ferrites offer the promising prospect of thermochemical looping H_2 production at < $2/kg-$H_2$ [52].

In both cases above, Fe is the redox active element. The H_2O/CO_2 splitting capacity of these ferrites comes from phase transformation, where one phase is oxygen-poor and the other is oxygen-rich. In CO_2 splitting thermochemical looping cycle, a larger phase swing between thermal/chemical reduction and CO_2 splitting conditions gives a higher CO_2 splitting capacity. For Fe-Co-O, Fe-Ni-

O and Fe-Mg-O systems, under thermal reduction based thermochemical looping conditions, the oxygen-poor phase is usually rocksalt and the oxygen-rich phase is spinel; when doing chemical reduction based thermochemical looping, the phases can be an oxygen-poor metallic phase and an oxygen-rich spinel phase [53–55]. Van't Hoff analysis was conducted on these ferrites to derive h_O and s_O [51]. However, the fundamental reasons that cause the counterintuitive dependence of CO_2 splitting capacity on the Fe ratio remain unidentified.

Here, we analyze the thermodynamic driving forces in Fe-poor (represented by $Fe_{0.45}Co_{0.55}O_{x_1}$) and Fe-rich (represented by $Fe_{2/3}Co_{1/3}O_{x_2}$, namely, $CoFe_2O_{3x_2}$) ferrites during thermochemical looping cycles. By means of CALPHAD-FactSage simulations [56], we find that the change in partial molar entropy s_O with oxygen stoichiometry x is determined primarily by cation configurational entropy for these ternary ferrites. We computed the other main entropy component, lattice vibrational entropy, via Hubbard-corrected density functional theory (DFT), known as DFT+U [57–60]. Additionally, we analyzed a generic phase diagram of two-phase systems to derive the optimal Fe ratio for maximal CO_2 splitting capacity, illuminating the significance of phase boundary positions. Finally, we built a reduced Gibbs free energy model to illustrate fundamental thermodynamic factors that influence the CO_2 splitting capacity.

Results and discussion

1. Entropic driving force in ternary ferrites

In this section, we extract thermodynamic equilibrium properties of the metal oxide from the CALPHAD database, the accuracy of which we verified by our own thermogravimetric measurements and elemental analyses (see **Figs. S1-S2, Table S1**, and **Subsections 1-4 in Supplementary Text of Electronic Supplementary Information (ESI)**). The thermodynamic requirements for reactions (1)/(3) and (4) to proceed are [51]

$$(-h_O) < T_H(-s_O) - \frac{1}{2}\left(H^\circ_{O_2} - T_H\left[S^\circ_{O_2} - \text{Rln}\frac{p_{O_2}}{p^{ref}}\right]\right) \tag{5}$$

where p_{O_2} is the (equivalent) oxygen partial pressure during thermal or chemical reduction.

and

$$(-h_0) > T_L(-s_0) - \left(H^\circ_{CO_2} - H^\circ_{CO}\right) + T_L\left[S^\circ_{CO_2} - S^\circ_{CO} - R\ln\frac{p_{CO_2}}{p_{CO}}\right] \tag{6}$$

where p_{CO_2} and p_{CO} are partial pressures of CO_2 and CO, and the partial molar properties are defined as

$$h_0(x_1) = \lim_{x_2\to x_1}\frac{H_{MO_{x_1}} - H_{MO_{x_2}}}{x_1 - x_2}$$

and

$$s_0(x_1) = \lim_{x_2\to x_1}\frac{S_{MO_{x_1}} - S_{MO_{x_2}}}{x_1 - x_2}$$

Expressions (5) and (6) have a linear form of $(-h_0)$ vs. $(-s_0)$ (red and blue lines, respectively, in **Figs. 1C-1D**). In the plane of $(-h_0)$ vs. $(-s_0)$, if the properties of an active oxide MO_x lie below the red line formed by (5), it can be reduced until the oxygen content x reaches a value such that an equality of (5) would hold; if an MO_x lies above the blue line formed by (6), it can get oxidized by CO_2 and produce CO at temperature T_L until x reaches a value such that the equality of (6) holds. Temporarily neglecting the temperature dependence of h_0 and s_0, the purple area formed by these two lines is the thermodynamically feasible zone of the thermochemical looping cycle.

The case of a thermal reduction based cycle is used in this subsection for illustration purposes. **Figs. 1A-1B** depict an equilibrium cycle constructed to separate temperature change and oxygen exchange, though the equilibrium cycle does not exactly reflect a real reaction pathway of a thermochemical looping cycle in practice. Solid red and blue curves in **Figs. 1A-1B** correspond to the representative Fe-poor (panel **A**) and Fe-rich (panel **B**) ferrites at T_H and T_L, respectively. In the equilibrium cycle, a ferrite heats up from state 1 to state 2 (yellow circles denoting states discussed) with a constant oxygen stoichiometry x and then isothermally releases O_2 at T_H to reach state 3; afterwards, the reduced ferrite cools down to state 4 with a constant x and then isothermally

splits CO_2 at T_L to get back to state 1. Since state 3 has the same solid-state oxygen to metal ratio as state 4, the thermodynamic equilibrium CO_2 splitting capacity is defined as the change of x in MO_x between states 1 and 3. In **Fig. 1**, state 1 has $T_L = 800$ °C and $\frac{p_{CO}}{p_{CO_2}} = 1:400$ ($p_{O_2} = 10^{-13.25}$ atm), and state 3 has $T_H = 1300$ °C and $p_{O_2} = 10^{-5}$ atm. Given a temperature, $\frac{p_{CO}}{p_{CO_2}}$ corresponds to an equivalent p_{O_2} via the equilibrium of $CO_2 \rightleftharpoons \frac{1}{2}O_2 + CO$. Simple inspection of the specific case drawn in **Figs. 1A-1B** reveals that the thermodynamic equilibrium CO_2 splitting capacity of $Fe_{0.45}Co_{0.55}O_{x_1}$ is about 50% larger than that of $Fe_{2/3}Co_{1/3}O_{x_2}$: The change of x for the Fe-poor ferrite is 0.6, and that for the Fe-rich ferrite is 0.4.

The equilibrium cycle can be visualized in the plot of thermodynamic requirements of reactions (1) and (4), which illustrates the thermodynamic driving force of these reactions. In **Figs. 1C-1D**, the set of dots connected by line segments show h_O and s_O of ferrites at 1300 °C (red) and 800 °C (blue), where the change of x between two neighboring dots is a constant of 0.0035 (mol-O/mol-M) for MO_x. The h_O vs. s_O trajectories show a strong dependence on temperature, and the dots connected by line segments should only be compared against the line for the same temperature. Despite the temperature mismatch, the dot for state 4 happens to be close to the 1300 °C straight line, and the dot for state 2 is close to the 800 °C line (especially for the Fe-poor ferrite in **Fig. 1C**). This shows that neglecting the temperature dependence of h_O and s_O when using diagrams like **Figs. 1C-1D** can still give a relatively accurate estimation of thermodynamic equilibrium CO_2 splitting capacity, as often seen in published van't Hoff analyses [44,51]. In general, for a material whose dots are dense in the thermodynamically feasible zone, its h_O and s_O properties remain feasible for the two-step cycle across a large range of x, leading to a large thermodynamic equilibrium CO_2 splitting capacity. The density of dots between 1 and 4 and between 2 and 3 is higher for $Fe_{0.45}Co_{0.55}O_{x_1}$ than for $Fe_{2/3}Co_{1/3}O_{x_2}$, and therefore, $Fe_{0.45}Co_{0.55}O_{x_1}$ has a higher oxygen exchange capacity because of a larger range of x, giving a larger total entropy of reduction.

Since analyzing the source and change of s_O is critical for directing materials design as mentioned in the **Introduction**, we compare the contribution from cation configurational entropy to the partial molar entropy of oxygen, $s_{O, config}$, against s_O in **Figs. 1E-1H**.

$$s_{0,config}(x_1) = \lim_{x_2 \to x_1} \frac{S_{config,MO_{x_1}} - S_{config,MO_{x_2}}}{x_1 - x_2}$$

where S_{config,MO_x} is the cation configurational entropy of MO_x, assuming random mixing of Fe^{2+}, Fe^{3+}, Co^{2+} and Co^{3+} cations within each type of site (rocksalt octahedral, spinel tetrahedral, and spinel octahedral sites). Thus $s_{0,config}(x)$ represents partial molar cation configurational entropy of oxygen.

The change of s_O with x is similar to that of $s_{O,config}$ at both 800 °C (**Figs. 1E-1F**) and 1300 °C (**Figs. 1G-1H**). Therefore, the dense dots in **Fig. 1C** of the high-capacity Fe-poor ferrite $Fe_{0.45}Co_{0.55}O_{x_1}$ originates from the slow change of s_O and h_O with x, and the change of s_O is largely determined by the cation configurational entropy.

Note that among the two phases that exist in equilibrium, spinel and rocksalt, the rocksalt phase exhibits higher configurational entropy than spinel because of the distribution of four distinct metallic species over a larger number of degenerate cation sites. Specifically, rocksalt has 33% more cation sites than spinel per O and all cation sites in rocksalt are octahedral while spinel has a distinct set of tetrahedral and octahedral cation sub-lattices. Hence, if a higher amount of the rocksalt phase emerges during thermal reduction, the resultant larger change in cation configurational entropy will drive up the overall entropy change in the solid.

2. First-principles calculation of vibrational entropy

To evaluate the contribution of vibrational entropy to the overall entropy change upon thermal reduction and/or CO_2 splitting, we obtained the phonon density of states via DFT+U calculations (see **Subsection 5 in Supplementary Text of ESI** and **Fig. S3** for details). The initial lattice parameters of both the rocksalt and spinel phases came from synchrotron X-ray diffraction data of quenched materials (**Fig. S4**), described in **Subsection 6 in Supplementary Text of ESI**. Specifically, we calculated the molar vibrational entropy (S_{vib}, see **Fig. 2A**), normalized per mole of oxygen, for the rocksalt and spinel compositions that correspond to states 1 and 3 in **Figs. 1A and 1B**. We based our S_{vib} calculations on special quasirandom structures (SQSs) [61], since both the rocksalt and spinel phases are disordered at T_H and T_L (**Fig. S5**). We chose the specific

compositions of the spinel and rocksalt at the two different temperatures to minimize errors against CALPHAD-simulated compositions at the corresponding temperatures (**Fig. S6, Table S2**). The vertical dotted red lines in **Fig. 2A** correspond to the thermal reduction and CO_2-splitting temperatures, while solid (dashed) lines indicate the solid phases with compositions corresponding to T_L (T_H). Importantly, the S_{vib} for the rocksalt phase is always higher than the corresponding spinel phase at all temperatures considered, which is consistent with the fact that rocksalt has more atoms per O (nominal stoichiometry of MO, where M = Fe, Co) than the spinel ($M_{0.75}O$). **Fig. 2B** displays the contribution of S_{vib} to the solid entropy change as the ferrite is heated and reduced from state 1 to state 3, along with the total entropy changes and cation configurational entropy changes obtained from CALPHAD simulations. Although the total solid entropy change of the rocksalt+spinel two-phase state is quite similar between Fe-poor and Fe-rich ferrites, the contribution of S_{vib} is lower in Fe-poor compared to Fe-rich ferrites, highlighting that configurational entropy is the predominant entropic driver in Fe-poor ferrites for the two-step cycle, as it has the same trend as the total entropy change.

3. Predicting the optimal iron ratio from phase diagrams

Here we develop a generic phase diagram analysis method that predicts the optimal metal composition for maximizing phase swing in phase transformation reactions. In the case of thermal reduction based thermochemical looping, we can predict the optimal Fe ratio for high CO_2 splitting capacity by analyzing phase diagrams like those of **Fig. 3A**, which displays the spinel-rocksalt phase boundaries of the Fe-Co-O system at 1300 °C and 800 °C. The two horizontal dashed lines are at $p_{O_2} = 10^{-5}$ atm for thermal reduction (top panel) and $p_{O_2} = 10^{-13.25}$ atm (CO:CO_2 = 1:400) for CO_2 splitting (bottom panel).

A large phase swing is desirable, so the optimal Fe ratio should occur in the two-phase region with boundaries delineated by the two vertical dashed lines in **Fig. 3A**. For an arbitrary Fe ratio y (such as the vertical solid purple line), the rocksalt phase fraction is $\frac{m}{|AB|}$ at the thermal reduction condition,

T_H, and drops to $\frac{n}{|CD|}$ at the CO_2 splitting condition, T_L. $|AB|$ and $|CD|$ are the extents of the miscibility gap at T_H and T_L, respectively. The goal is to maximize the phase fraction swing,

$$\phi = \frac{m}{|AB|} - \frac{n}{|CD|} = \frac{n + m_0}{|AB|} - \frac{n}{|CD|} = n\left(\frac{1}{|AB|} - \frac{1}{|CD|}\right) + \frac{m_0}{|AB|} \tag{6}$$

Equation (6) shows that ϕ is a linear function of n, which can take any value from 0 to $|CD| - n_0$ in the two-phase region. Then the sign of $\left(\frac{1}{|AB|} - \frac{1}{|CD|}\right)$ determines the n value that maximizes ϕ. For **Fig. 3A**, $\frac{1}{|AB|} - \frac{1}{|CD|} > 0$, which is typical for most systems since the extent of miscibility gap tends to decrease in size as temperature increases. Hence, $n = n_{max} = |CD| - n_0$ gives the optimal Fe ratio, which occurs at the rocksalt phase boundary of the 1300 °C phase diagram. In other words, given temperature and p_{O_2} conditions for thermal reduction and CO_2 splitting reactions, the maximum CO_2 splitting capacity, ϕ_{max}, will be achieved if the overall Fe ratio of the two-phase system coincides with that of the rocksalt (oxygen-poor) phase boundary at the thermal reduction condition, T_H.

The phase diagram analysis above accurately predicts the optimal Fe ratio, shown in **Figs. 3B-3D** and **Fig. S7** for Fe-Co-O, Fe-Ni-O and Fe-Mg-O. The vertical dashed black lines indicate the optimal Fe ratios predicted by the phase diagram analysis. The curves are thermodynamic equilibrium CO_2 splitting capacities from the CALPHAD model, represented by the change of oxygen stoichiometry, Δx, between thermal reduction and CO_2 splitting conditions (**Subsection 4 in Supplementary Text of ESI**). Different curve colors correspond to different $CO:CO_2$ ratios. Just as indicated by the phase diagram analysis above, the optimal Fe ratio depends on the thermal reduction condition but not on the $CO:CO_2$ ratio of the CO_2 splitting step. Importantly, our phase diagram analysis correctly predicts the composition corresponding to the maximal capacity, which occurs at the rocksalt phase boundary at T_H.

Combining the phase diagram analysis results in **Fig. 3** and **Fig. S7**, we can tell that the best spinel/rocksalt Fe-M-O materials need to have the following: (i) at T_L, the phase boundary between rocksalt (MO-rich) and spinel (Fe_3O_4-rich) should be as wide as possible. This would give a large $|CD|$. (ii) at T_H, rocksalt phase MO has as high solubility of FeO as possible. This would give a small $|AB|$.

The CO:CO$_2$ ratios when analyzing the thermal reduction based thermochemical looping above are generally too small for practical CO$_2$ splitting applications. On the other hand, CO:CO$_2$ ratios and the corresponding (equilibrium) CO$_2$ conversions are much higher in the case of chemical reduction based thermochemical looping. For such a cycle at T$_{\text{Looping}}$ = 700 °C, we use the phase diagram **Fig. 4A** where BCC and FCC metallic phases are merged into a single region just for the purpose of the current analysis. The original full phase diagram is given in **Fig. S8**. The chemical reduction condition is p_{O_2} = 10$^{-20.5}$ atm, a typical value with a reducing agent present [52]. Two CO$_2$ splitting conditions used in this study are p_{O_2} = 10$^{-18.5}$ atm (CO:CO$_2$ = 1:24, equilibrium CO$_2$ conversion = 4%), and p_{O_2} = 10$^{-19.5}$ atm (CO:CO$_2$ = 1:8, equilibrium CO$_2$ conversion = 11.1%). Note here that the chemical reduction and CO$_2$ splitting happen with the spinel+metal phase combination instead of the spinel+rocksalt combination. Nevertheless, the expression (6) for phase ratio swing still holds in this case. For **Fig. 4A**, $\frac{1}{|AB|} - \frac{1}{|CD|} > 0$, therefore, $n = n_{max} = |CD| - n_0$ gives the optimal Fe ratio, which occurs where the metals phase boundary crosses the line for chemical reduction p_{O_2}. Our phase diagram analysis correctly predicts the optimal metal composition as **Fig. 4B** shows.

Because this approach does not require information on oxygen stoichiometry, such predictions that are based on inspecting phase diagrams can expedite both materials searches for the maximal oxygen exchange capacity as well as the selection of thermal/chemical reduction and CO$_2$ splitting conditions. Additionally, the analysis above highlights the importance of miscibility gap in materials design, so strategies to tune phase boundary and miscibility gap such as size effects [62,63] and cation mixing [64,65] may be utilized to improve the CO$_2$ splitting capacity of phase swing materials.

4. Reduced Gibbs free energy model

The previous section showed that phase boundary positions determine the maximal phase fraction swing of a two-phase material for thermochemical looping water/CO$_2$ splitting, while the phase swing in turn determines the water/CO$_2$ splitting capacity. Hence, connecting material

thermodynamic parameters with phase boundary positions should help uncover the critical parameters for CO_2 splitting capacity improvement.

Inspired by the phase diagram analysis in **Fig. 3A**, we develop a simple approach to determine the phase diagram by using the following Gibbs free energy (G) function for spinel and rocksalt phases in Fe-Co-O, Fe-Ni-O, and Fe-Mg-O systems. For each phase at a specific temperature, we used the following relation to fit the CALPHAD-based Gibbs energy plotted in **Figs. S9-S11**:

$$G = C + \Delta G y + RT[y\ln y + (1-y)\ln(1-y)] + [\beta_1 y + \beta_2(1-y)]y(1-y) + \alpha RT y \log_{10} p_{O_2}$$

G is the Gibbs energy of the solid phase (per mole of metal) which depends on y (the Fe ratio) and $\log_{10} p_{O_2}$, resulting in a 3D "G surface". Here a binary sub-regular solution model was used to approximate the CALPHAD model of spinel and rocksalt phases with four types of cations (Fe^{2+}, Fe^{3+}, Co^{2+} and Co^{3+}) plus cation vacancies. The fitting parameters have the following physical meanings: C determines the global position of the G surface; ΔG is the difference in Gibbs energy between the two end members of $y = 0$ and $y = 1$; β_1 and β_2 are sub-regular solution model parameters; and α captures the sensitivity of G with respect to p_{O_2} variation. This simplified form fits the CALPHAD data reasonably well (**Figs. S12-S14**). The mechanisms of G variation with p_{O_2} include Fe redox reactions and the change of solid-state oxygen-to-metal ratio, with details for the latter in the **Subsection 7 in Supplementary Text of ESI**.

Using the reduced model, we constructed tie lines between the spinel and rocksalt phases to give the phase boundaries at the p_{O_2} and temperatures for thermal reduction (T_H = 1300 °C and p_{O_2} = 10^{-5} atm) and CO_2 splitting (T_L = 800 °C and p_{O_2} = 10^{-13} atm) conditions (**Subsection 8 in Supplementary Text of ESI** and **Figs. S15-S16** explain the method). Thereafter, the optimal Fe ratio that produces the maximal swing in phase fraction can be extracted from the phase diagram analysis described in the previous section. Then, we undertook a sensitivity analysis by artificially changing each model parameter independently by up to ±10%. **Fig. 5** and **Figs. S17-S18** display the resultant variations in the maximal phase fraction swing for Fe-Co-O, Fe-Ni-O, and Fe-Mg-O. Improving the CO_2 splitting capacity requires increasing the phase fraction swing (red color in **Fig. 5**), which for Fe-Co-O occurs most significantly when ΔG (affected by end member choices) increases for the rocksalt phase at T_H before entering unfeasible grey regions in **Fig. 5**, when ΔG decreases for the spinel phase at T_H, and when α (affected by cation redox at varied p_{O_2}) decreases

for the rocksalt phase at T_H. Often, when large artificial changes of parameters are applied, a common tangent tie line cannot be found for the G curves (indicated by grey boxes), which suggests that the artificial material would enter a single-phase regime in the two-step cycle. Overall, the results of **Fig. 5** suggest that tuning thermodynamic parameters at T_H of thermal reduction is more impactful on the CO_2 splitting capacity than tuning parameters at T_L. Since entropic effects are more significant at higher temperatures, entropic tuning of oxides by methods like cation mixing is desirable when exploring materials for improved thermochemical cycle (TCC) performance.

Conclusions

We analyzed thermodynamic driving forces here by CALPHAD simulations and DFT+U calculations for Fe-Co-O as an example of a phase transformation material for thermochemical looping water/CO_2 splitting. We expressed the thermodynamic requirements for reactions in the thermochemical looping cycle in terms of partial molar properties of the metal oxide, where the temperature dependence of partial molar properties was considered to separate the effects of temperature and phase change. We compared examples of Fe-poor and Fe-rich ferrites in the same thermodynamic framework, where the change in partial molar properties with oxygen stoichiometry determines the thermodynamic equilibrium water/CO_2 splitting capacity. Specifically, we showed that cation configurational entropy determines the change of partial molar entropy with oxygen stoichiometry. The other main contributor to solid-state entropy is lattice vibration, calculated here by DFT+U theory.

We used a generic phase diagram analysis to find the optimal Fe ratio to maximize the water/CO_2 splitting capacity of two-phase materials including ternary ferrites. The optimal Fe ratio predicted by the phase diagram analysis is consistent with CALPHAD calculations of oxygen stoichiometry swing in both thermal reduction based and chemical reduction based thermochemical looping cycles. With chemical reduction, >10% CO_2 conversion and high oxygen exchange capacity can both be achieved. Finally, we developed a reduced Gibbs free energy model to determine the critical thermodynamic parameters that affect CO_2 splitting performance of Fe-Co-O, Fe-Ni-O, and Fe-Mg-O systems.

This work focuses on the thermodynamics of phase swing materials; for practical applications of thermochemical looping cycles, kinetics and cyclability are also important factors affecting final product cost, so strategies for improving those performances are worth investigating. Overall, our research uncovered the thermodynamic driving forces underpinning high-capacity Fe-poor ferrites and further explained the phenomenon via phase diagram analysis. Future materials improvement can be guided by our reduced Gibbs energy model.

Author contributions

Conceptualization: SZ, AM, WCC

Methodology: all authors

Investigation: SZ, JN, GSG, KL, JR

Visualization: SZ, GSG

Supervision: AM, WCC, IHJ, EAC, MFT

Writing—original draft: SZ, JN, GSG, KL, IHJ

Writing—review & editing: all authors

Conflicts of interest

There are no conflicts of interest to declare.

Acknowledgements

Office of Energy Efficiency and Renewable Energy located at National Renewable Energy Laboratory.

References

1   United States Environmental Protection Agency, Global Greenhouse Gas Emissions Data, https://www.epa.gov/ghgemissions/global-greenhouse-gas-emissions-data.

2   R. Lindsey, CO2 in the atmosphere and annual emissions (1750-2019), https://www.climate.gov/news-features/understanding-climate/climate-change-atmospheric-carbon-dioxide.

3   M. Joshi, E. Hawkins, R. Sutton, J. Lowe and D. Frame, *Nat. Clim. Chang.*, 2011, **1**, 407.

4   UNFCCC. Conference of the Parties (COP), *Paris Climate Change Conference-November 2015, COP 21*, 2015.

5   B. Walsh, P. Ciais, I. A. Janssens, J. Peñuelas, K. Riahi, F. Rydzak, D. P. van Vuuren and M. Obersteiner, *Nat. Commun.*, 2017, **8**, 14856.

6   N. MacDowell, N. Florin, A. Buchard, J. Hallett, A. Galindo, G. Jackson, C. S. Adjiman, C. K. Williams, N. Shah and P. Fennell, *Energy Environ. Sci.*, 2010, **3**, 1645–1669.

7   Y. Gao, X. Gao and X. Zhang, *Engineering*, 2017, **3**, 272–278.

8   S. Chu, Y. Cui and N. Liu, *Nat. Mater.*, 2016, **16**, 16.

9   S. Fuss, J. G. Canadell, G. P. Peters, M. Tavoni, R. M. Andrew, P. Ciais, R. B. Jackson, C. D. Jones, F. Kraxner, N. Nakicenovic, C. Le Quéré, M. R. Raupach, A. Sharifi, P. Smith and Y. Yamagata, *Nat. Clim. Chang.*, 2014, **4**, 850–853.

10   S. Fuss, W. F. Lamb, M. W. Callaghan, J. Hilaire, F. Creutzig, T. Amann, T. Beringer, W. de Oliveira Garcia, J. Hartmann, T. Khanna, G. Luderer, G. F. Nemet, J. Rogelj, P. Smith, J. L. V. Vicente, J. Wilcox, M. del Mar Zamora Dominguez and J. C. Minx, *Environ. Res. Lett.*, 2018, **13**, 63002.

11   M. Kayfeci, A. Keçebaş and M. Bayat, in *Solar Hydrogen Production*, eds. F. Calise, M. D. D'Accadia, M. Santarelli, A. Lanzini and D. Ferrero, Academic Press, 2019, pp. 45–83.

12   P. Breeze, in *Power System Energy Storage Technologies*, ed. P. Breeze, Academic Press, 2018, pp. 69–77.

13   O. Schmidt, A. Gambhir, I. Staffell, A. Hawkes, J. Nelson and S. Few, *Int. J. Hydrogen Energy*, 2017, **42**, 30470–30492.

14   M. Carmo, D. L. Fritz, J. Mergel and D. Stolten, *Int. J. Hydrogen Energy*, 2013, **38**, 4901–4934.

15   M. A. Khan, H. Zhao, W. Zou, Z. Chen, W. Cao, J. Fang, J. Xu, L. Zhang and J. Zhang, *Electrochem. Energy Rev.*, 2018, **1**, 483–530.

16   C. Jiang, S. J. A. Moniz, A. Wang, T. Zhang and J. Tang, *Chem. Soc. Rev.*, 2017, **46**, 4645–4660.

17   J. H. Kim, D. Hansora, P. Sharma, J.-W. Jang and J. S. Lee, *Chem. Soc. Rev.*, 2019, **48**, 1908–1971.

18   T. Sakakura, J.-C. Choi and H. Yasuda, *Chem. Rev.*, 2007, **107**, 2365–2387.

19   Z. Jiang, T. Xiao, V. L. Kuznetsov and P. P. Edwards, *Philos. Trans. R. Soc. London A Math. Phys. Eng. Sci.*, 2010, **368**, 3343–3364.

20   W. Wang, S. Wang, X. Ma and J. Gong, *Chem. Soc. Rev.*, 2011, **40**, 3703–3727.

21   Q. Liu, L. Wu, R. Jackstell and M. Beller, *Nat. Commun.*, 2015, **6**, 5933.

22   M. D. Porosoff, B. Yan and J. G. Chen, *Energy Environ. Sci.*, 2016, **9**, 62–73.

23   T. P. Senftle and E. A. Carter, *Acc. Chem. Res.*, 2017, **50**, 472–475.

24   A. Majumdar and J. Deutch, *Joule*, 2018, **2**, 805–809.

25   C. Hepburn, E. Adlen, J. Beddington, E. A. Carter, S. Fuss, N. Mac Dowell, J. C. Minx, P. Smith and C. K. Williams, *Nature*, 2019, **575**, 87–97.

26   L.-S. Fan, *Chemical Looping Systems for Fossil Energy Conversions*, John Wiley & Sons, Ltd, 2010.

27   L.-S. Fan, *Chemical Looping Partial Oxidation: Gasification, Reforming, and Chemical Syntheses*, Cambridge University Press, 2017.

28   L. Zeng, Z. Cheng, J. A. Fan, L.-S. Fan and J. Gong, *Nat. Rev. Chem.*, 2018, **2**, 349–364.

29   Ronald W. Breault, Ed., *Handbook of Chemical Looping Technology*, John Wiley & Sons, Ltd, 2018.

30   W. C. Chueh, C. Falter, M. Abbott, D. Scipio, P. Furler, S. M. Haile and A. Steinfeld, *Science (80-.)*, 2010, **330**, 1797–1801.

31   J. R. Scheffe and A. Steinfeld, *Mater. Today*, 2014, **17**, 341–348.

32   R. J. Carrillo and J. R. Scheffe, *Sol. Energy*, 2017, **156**, 3–20.

33   S. Li, P. B. Kreider, V. M. Wheeler and W. Lipiński, *J. Sol. Energy Eng.*, 2019, **141**, 021012.

34   D. Arifin, A. Ambrosini, S. A. Wilson, B. Mandal, C. L. Muhich and A. W. Weimer, *Int. J. Hydrogen Energy*, 2020, **45**, 160–174.

35   G. Sai Gautam, E. B. Stechel and E. A. Carter, *Adv. Theory Simulations*, 2020, **3**, 2000112.

36   T.-L. Hsieh, D. Xu, Y. Zhang, S. Nadgouda, D. Wang, C. Chung, Y. Pottimurthy, M. Guo, Y.-Y. Chen, M. Xu, P. He, L.-S. Fan and A. Tong, *Appl. Energy*, 2018, **230**, 1660–1672.

37   X. Zhu, K. Li, L. Neal and F. Li, *ACS Catal.*, 2018, **8**, 8213–8236.

38   M. Luo, Y. Yi, S. Wang, Z. Wang, M. Du, J. Pan and Q. Wang, *Renew. Sustain. Energy Rev.*, 2018, **81**, 3186–3214.

39   J. Yang, N. Cai and Z. Li, *Energy & Fuels*, 2008, **22**, 2570–2579.

40   Y. Feng, N. Wang, X. Guo and S. Zhang, *Fuel*, 2020, **262**, 116489.

41   A. Thursfield, A. Murugan, R. Franca and I. S. Metcalfe, *Energy Environ. Sci.*, 2012, **5**, 7421–7459.

42   P. Furler, D. Marxer, M. Takacs, A. Steinfeld, R. Mancilla and C. Richter, *AIP Conf. Proc.*, 2018, **2033**, 130005.

43   B. Meredig and C. Wolverton, *Phys. Rev. B - Condens. Matter Mater. Phys.*, 2009, **80**, 1–8.

44   J. E. Miller, A. H. McDaniel and M. D. Allendorf, *Adv. Energy Mater.*, 2014, **4**, 1300469.

45   C. L. Muhich, S. Blaser, M. C. Hoes and A. Steinfeld, *Int. J. Hydrogen Energy*, 2018, **43**, 18814–18831.

46   I. Ermanoski and E. B. Stechel, *Sol. Energy*, 2020, **198**, 578–585.

47   T. C. Davenport, M. Kemei, M. J. Ignatowich and S. M. Haile, *Int. J. Hydrogen Energy*, 2017, **42**, 16932–16945.

48   I. A. Al-Shankiti, A. Bayon and A. W. Weimer, *Chem. Eng. J.*, 2020, **389**, 124429.

49   S. L. Millican, I. Androshchuk, J. T. Tran, R. M. Trottier, A. Bayon, Y. Al Salik, H. Idriss, C. B. Musgrave and A. W. Weimer, *Chem. Eng. J.*, 2020, **401**, 126015.

50   G. Sai Gautam, E. B. Stechel and E. A. Carter, *Chem. Mater.*, 2020, **32**, 9964–9982.

51   S. Zhai, J. Rojas, N. Ahlborg, K. Lim, C. H. M. Cheng, C. Xie, M. F. Toney, I.-H. Jung, W. C. Chueh and A. Majumdar, *Energy Environ. Sci.*, 2020, **13**, 592–600.

52   J. Rojas, V. Haribal, I.-H. Jung and A. Majumdar, *Cell Reports Phys. Sci.*, 2021, **2**, 100362.

53   I.-H. Jung, S. A. Decterov, A. D. Pelton, H.-M. Kim and Y.-B. Kang, *Acta Mater.*, 2004, **52**, 507–519.

54   M. A. Rhamdhani, P. C. Hayes and E. Jak, *Metall. Mater. Trans. B Process Metall. Mater. Process. Sci.*, 2008, **39**, 690–701.

55   I. H. Jung, S. A. Decterov and A. D. Pelton, *J. Phys. Chem. Solids*, 2004, **65**, 1683–1695.

56   C. W. Bale, E. Bélisle, P. Chartrand, S. A. Decterov, G. Eriksson, A. E. Gheribi, K. Hack, I.-H. Jung, Y.-B. Kang, J. Melançon, A. D. Pelton, S. Petersen, C. Robelin, J. Sangster, P. Spencer and M.-A. Van Ende, *Calphad*, 2016, **54**, 35–53.

57   V. I. Anisimov, J. Zaanen and O. K. Andersen, *Phys. Rev. B*, 1991, **44**, 943–954.

58   S. L. Dudarev, G. A. Botton, S. Y. Savrasov, C. J. Humphreys and A. P. Sutton, *Phys. Rev. B*, 1998, **57**, 1505–1509.

59   G. Sai Gautam and E. A. Carter, *Phys. Rev. Mater.*, 2018, **2**, 95401.

60   O. Y. Long, G. Sai Gautam and E. A. Carter, *Phys. Rev. Mater.*, 2020, **4**, 45401.

61   A. Zunger, S.-H. Wei, L. G. Ferreira and J. E. Bernard, *Phys. Rev. Lett.*, 1990, **65**, 353–356.

62   N. Meethong, H.-Y. S. Huang, W. C. Carter and Y.-M. Chiang, *Electrochem. Solid-State Lett.*, 2007, **10**, A134.

63   S. Yi, V. Attari, M. Jeong, J. Jian, S. Xue, H. Wang, R. Arroyave and C. Yu, *J. Mater. Chem. A*, 2018, **6**, 17559–17570.

64   S. Zhai, J. Rojas, N. Ahlborg, K. Lim, M. F. Toney, H. Jin, W. C. Chueh and A. Majumdar, *Energy Environ. Sci.*, 2018, **11**, 2172–2178.

65   Y. Gao, Y. Mao, Z. Song, X. Zhao, J. Sun, W. Wang, G. Chen and S. Chen, *Appl. Energy*, 2020, **279**, 115777.
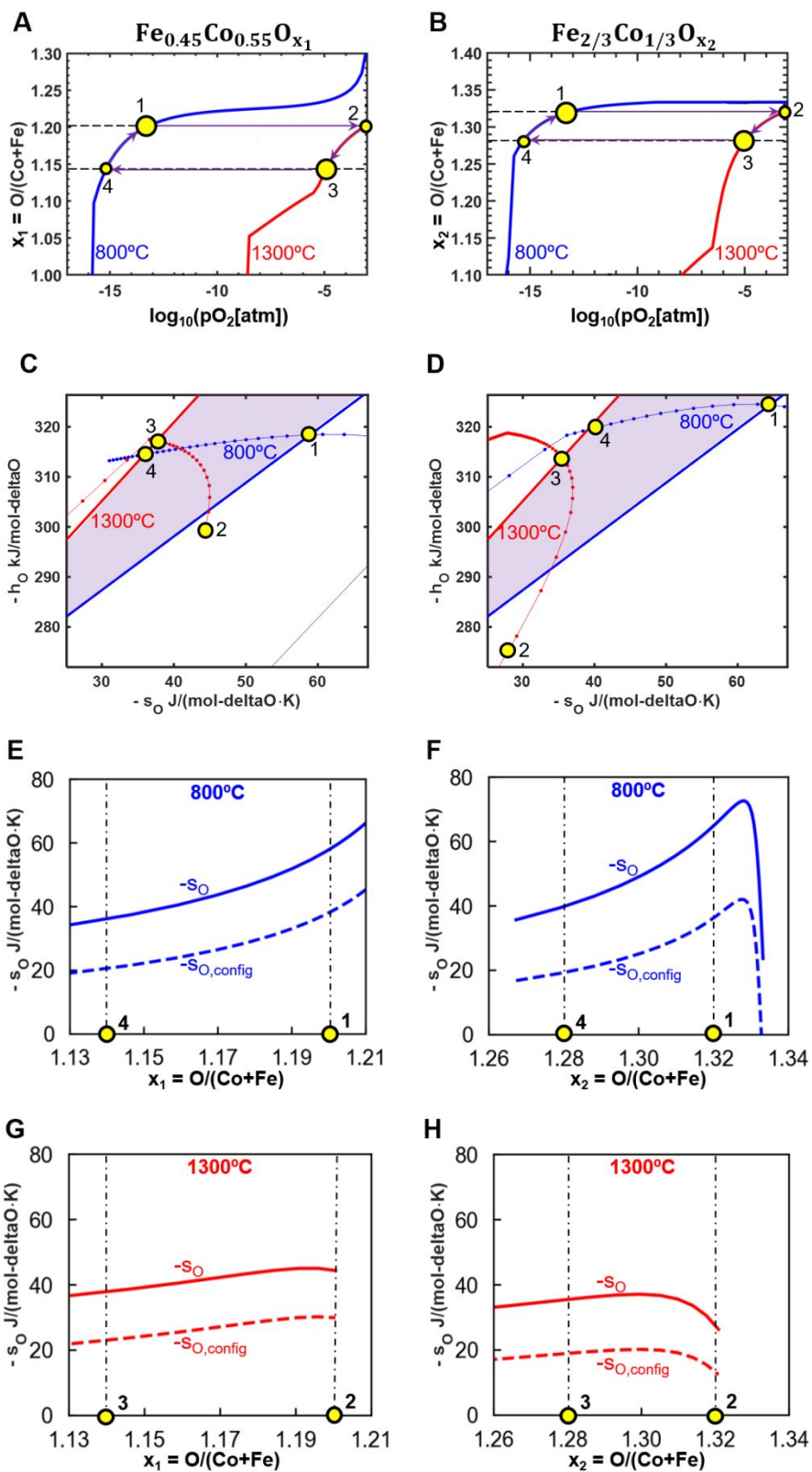
Figures

Fig. 1. Comparison between iron-poor and iron-rich ferrites for the entropic and enthalpic driving forces in a thermal reduction based equilibrium thermochemical looping cycle for CO_2 splitting. Ferrite thermodynamic data are from CALPHAD simulations (see **Subsection 4 in Supplementary Text of ESI**). **A**, **C**, **E** and **G** are for $Fe_{0.45}Co_{0.55}O_{x_1}$, while **B**, **D**, **F** and **H** are for $Fe_{2/3}Co_{1/3}O_{x_2}$. (**A-B**), isotherms of oxygen stoichiometry x versus oxygen partial pressure p_{O_2}. Condition 1 is $T_L = 800\ °C$ and $CO:CO_2 = 1:400$ ($p_{O_2} = 10^{-13.25}$ atm); condition 3 is $T_H = 1300\ °C$ and $p_{O_2} = 10^{-5}$ atm. In a thermal reduction based cycle, the material cycles between conditions 1 and 3, indicated by the big yellow circles. Conditions 2 and 4 are defined as having the same oxygen stoichiometry as 1 and 3, respectively, to form an equilibrium cycle. (**C-D**), red indicates 1300 °C and blue indicates 800 °C; the solid straight lines are generic partial molar properties of an oxide that achieves equilibrium at conditions 1 and 3, and the purple region is thermodynamically feasible for both thermal reduction and CO_2 splitting reactions. Each set of points connected by line segments forms an isotherm for varying p_{O_2}, where the difference in x between two neighboring points is 0.0035. (**E-F**), the change of partial molar entropy of oxygen s_O and partial molar cation configurational entropy of oxygen $s_{O,config}$ with oxygen stoichiometry x at 800 °C around conditions 1 and 4. (**G-H**), the change of s_O and $s_{O,config}$ with oxygen stoichiometry x at 1300 °C around conditions 2 and 3.
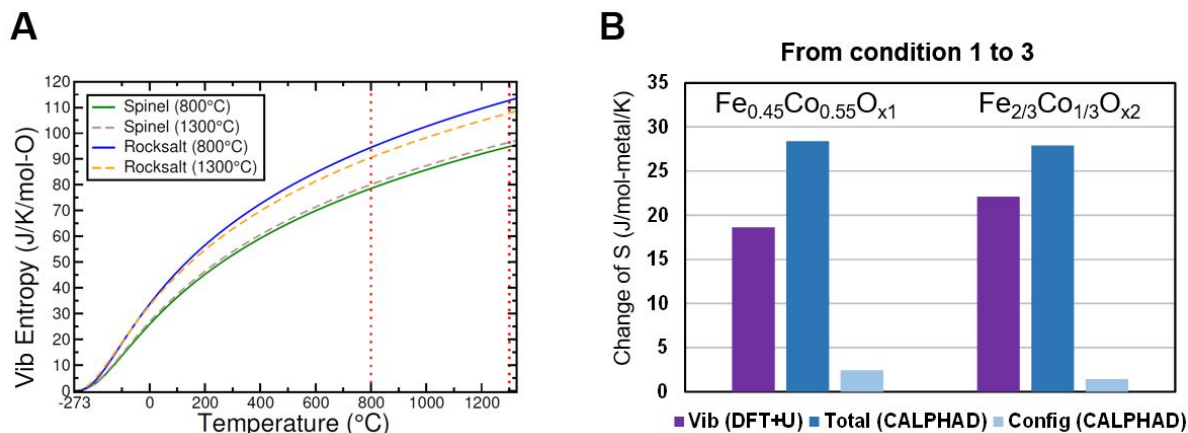
Fig. 2. Simulation of lattice vibrational entropy for thermal reduction based thermochemical looping. (**A**), the dependence of vibrational entropy on temperature, from DFT+U calculations on special quasirandom structure (SQS) models. These SQS models were set up with cation occupancies close to CALPHAD thermodynamic equilibrium simulations of thermal reduction (condition 3) and CO_2 splitting (condition 1) (see **Table S2**). The initial lattice parameters of the rocksalt and spinel phases for DFT+U calculations came from synchrotron X-ray diffraction measurements of quenched materials. (**B**), changes in entropy components and changes in total entropy going from condition 1 to 3 (See **Fig. 1** for definition of the conditions). The change of vibrational entropy is from DFT+U calculations while the changes in total solid entropy and in cation configurational entropy are from CALPHAD simulations. Note the entropy in panel **A** is normalized per mole of oxygen in a given solid phase (spinel or rocksalt), while the change in entropy in panel **B** is normalized per mole of metal in a spinel-rocksalt two-phase equilibrium.
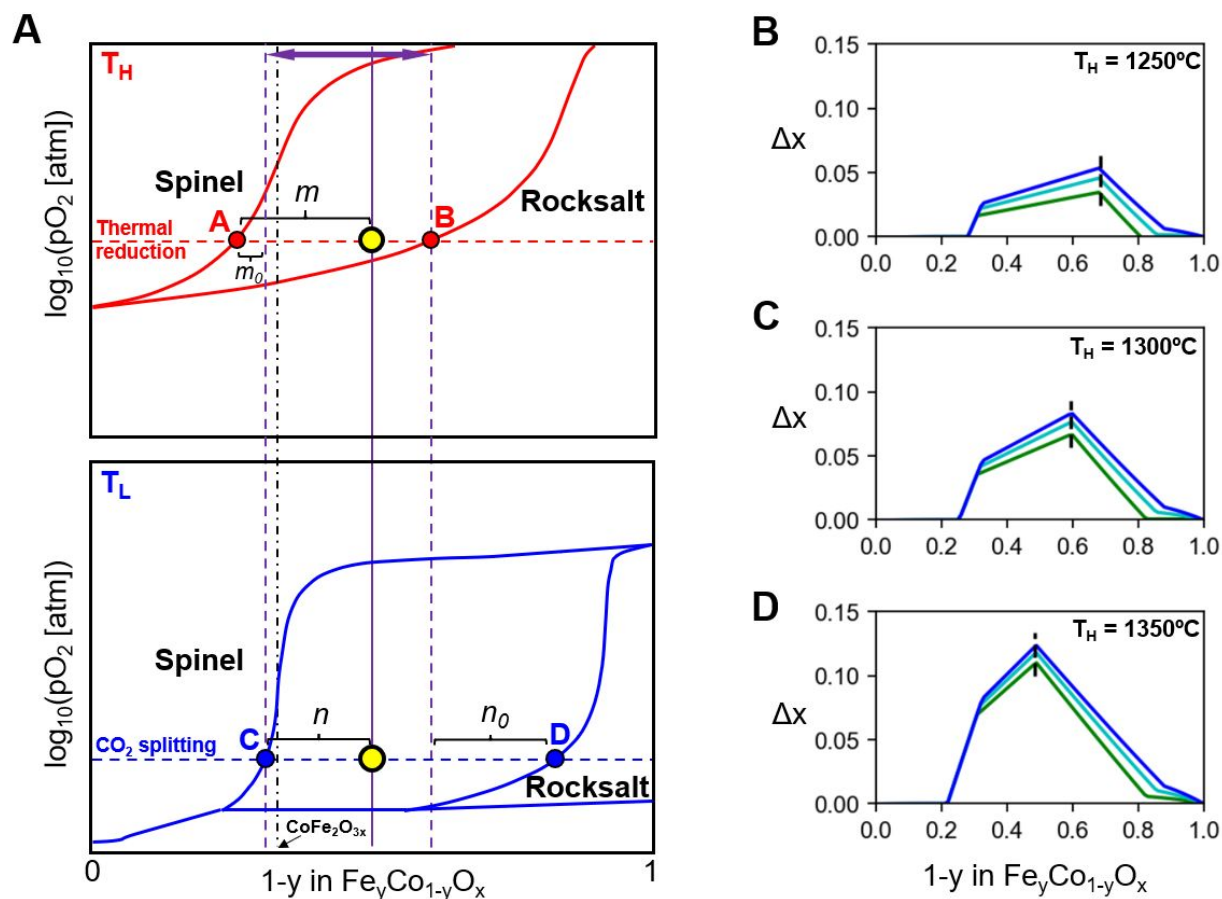
Fig. 3. Phase diagram explanation of the optimal metal composition to maximize the thermodynamic equilibrium capacity of ternary ferrites in thermal reduction based thermochemical looping CO_2 splitting. (**A**), phase boundaries and miscibility gap of the spinel and rocksalt phases in the Fe-Co-O system. Not all phase boundaries are shown. $T_H = 1300\ ^\circ C$ and $T_L = 800\ ^\circ C$ phase diagrams are used. Most values on the axes are omitted as the analysis method is generic. The horizontal dashed lines show the p_{O_2} for thermal reduction and CO_2 splitting reactions. The vertical dashed lines mark the considered range of metal compositions inside the two-phase looping regime. The vertical dash-dotted line is the traditional ferrite $CoFe_2O_{3x}$. (**B-D**), thermodynamic equilibrium CO_2 splitting capacity curves, expressed by the change of oxygen stoichiometry in ferrite materials, Δx, between thermal reduction and CO_2 splitting conditions. The vertical black dashed lines are the optimal metal compositions by the phase diagram analysis, which agree well with peaks of the capacity curves. These **B**, **C** and **D** are for thermal reduction conditions of $p_{O_2} = 10^{-5}$ atm and $T_H = 1250$, 1300 and 1350 °C, respectively. $T_L = 800\ ^\circ C$ is for the CO_2 splitting step and different CO_2-to-CO conversions are shown: the blue line is for $p_{O_2} =$

$10^{-11.49}$ atm (CO:CO$_2$ = 1:3000), the cyan line is p_{O_2} = $10^{-12.44}$ atm (CO:CO$_2$ = 1:1000), and the green line is p_{O_2} = $10^{-13.25}$ atm (CO:CO$_2$ = 1:400). The phase diagrams and thermodynamic data are from CALPHAD simulation of Fe-Co-O, but the analysis for the optimal metal composition can be applied to other phase transformation materials.
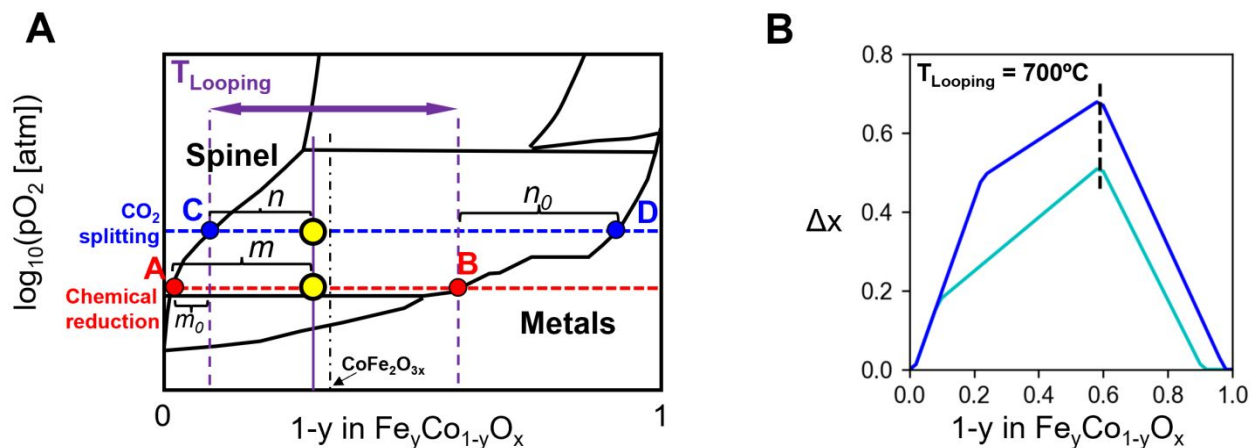
Fig. 4. Phase diagram explanation of the optimal metal composition to maximize the thermodynamic equilibrium capacity of ternary ferrites in chemical reduction based thermochemical looping CO_2 splitting. (**A**), phase boundaries and miscibility gap of the spinel and metallic phases in the Fe-Co-O system at $T_{Looping} = 700\ °C$. Not all phase boundaries are shown, and BCC and FCC metallic phases are merged into one region for analysis purposes. Most values on the axes are omitted as the analysis method is generic. The horizontal dashed lines show the p_{O_2} for chemical reduction and CO_2 splitting reactions. The vertical dashed lines mark the considered range of metal compositions inside two-phase looping regime. The vertical dash-dotted line is the traditional ferrite $CoFe_2O_{3x}$. (**B**), thermodynamic equilibrium CO_2 splitting capacity curves, expressed by the change of oxygen stoichiometry in ferrite materials, Δx, between chemical reduction and CO_2 splitting conditions. The vertical black dashed lines are the optimal metal compositions by the phase diagram analysis, which agree well with peaks of the capacity curves. The chemical reduction condition is $p_{O_2} = 10^{-20.5}$ atm and different CO_2 splitting conditions are shown: the blue line is $p_{O_2} = 10^{-18.5}$ atm ($CO:CO_2 = 1:24$, CO_2 equilibrium conversion 4%), and the cyan line is $p_{O_2} = 10^{-19.5}$ atm ($CO:CO_2 = 1:8$, CO_2 equilibrium conversion 11.1%). The phase diagrams and thermodynamic data are from CALPHAD simulation of Fe-Co-O, but the analysis for the optimal metal composition can be applied to other phase transformation situations.
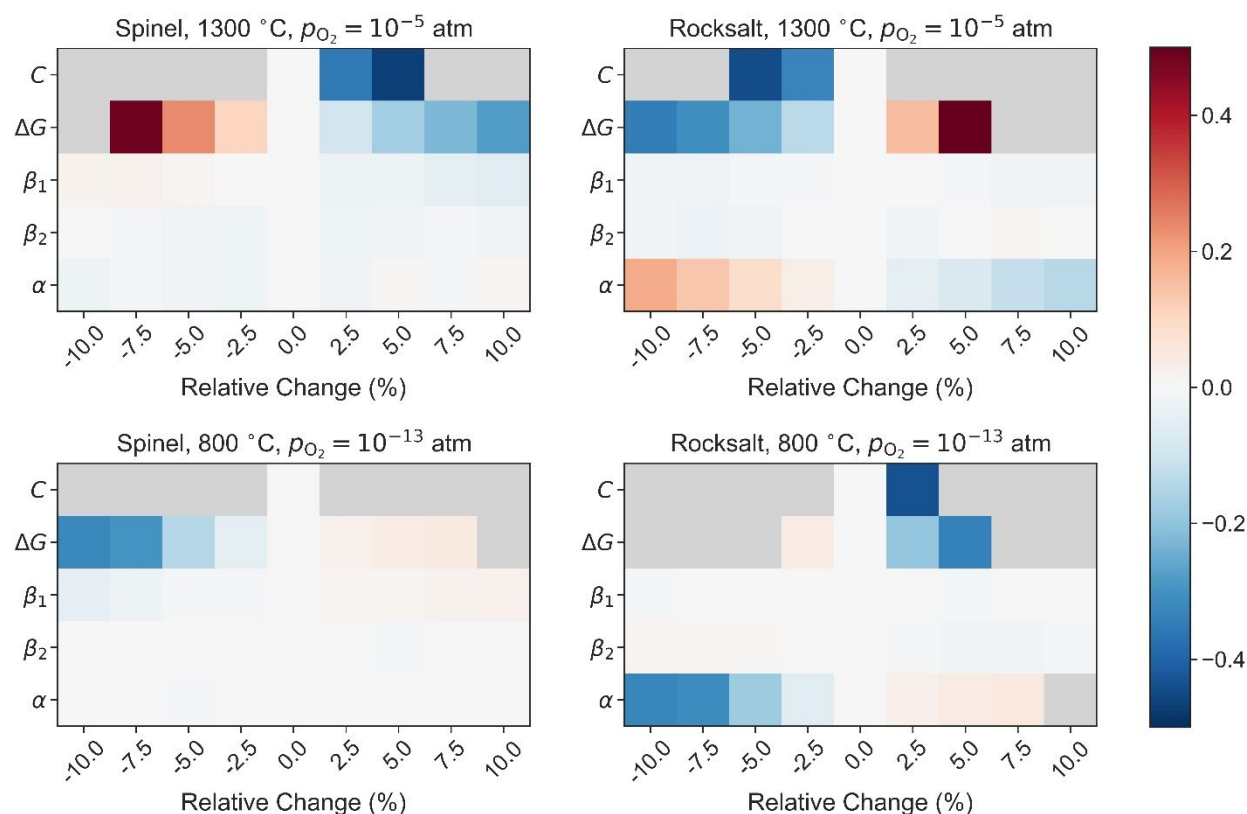
Fig. 5. Variations of the maximal phase fraction swing in the thermal reduction based thermochemical looping cycle, when artificially changing each parameter of the reduced Gibbs free energy model for the Fe-Co-O material system. The reaction conditions are thermal reduction at T_H = 1300 °C and p_{O_2} = 10⁻⁵ atm, and CO_2 splitting at T_L = 800 °C and p_{O_2} = 10⁻¹³ atm. Without artificial changes of any model parameter, the reduced G model gives the maximal phase fraction swing of 0.37 when the Fe ratio is 0.32. Then each model parameter was changed artificially by up to ±10% to investigate its influence on the maximal phase fraction swing. Grey boxes indicate that no common tangent tie line could be found for the G curves of rocksalt and spinel phases in those regions of model parameter changes.